Microstructural and optical properties of spinel oxide $M_xCo_{2-x}MnO_4$ (M = Ni, Zn or Cu; 0 < x < 1) thin films prepared by inorganic polycondensation and dip-coating methods

Thi Ly Le, Sophie Guillemet-Fritsch, Pascal Dufour, Christophe Tenailleau

PII: S0040-6090(16)30181-X
DOI: doi: 10.1016/j.tsf.2016.05.030
Reference: TSF 35213

To appear in: *Thin Solid Films*

Received date: 1 December 2015
Revised date: 12 May 2016
Accepted date: 19 May 2016

Please cite this article as: Thi Ly Le, Sophie Guillemet-Fritsch, Pascal Dufour, Christophe Tenailleau, Microstructural and optical properties of spinel oxide $M_xCo_{2-x}MnO_4$ (M = Ni, Zn or Cu; 0 < x < 1) thin films prepared by inorganic polycondensation and dip-coating methods, *Thin Solid Films* (2016), doi: 10.1016/j.tsf.2016.05.030

Microstructural and optical properties of spinel oxide $M_xCo_{2-x}MnO_4$ (M = Ni, Zn or Cu; 0 < x < 1) thin films prepared by inorganic polycondensation and dip-coating methods

Thi Ly Le[1], Sophie Guillemet-Fritsch[1], Pascal Dufour[1], Christophe Tenailleau[1,*]

[1]Laboratoire CIRIMAT, UMR CNRS 5085, Université de Toulouse, 118 Route de Narbonne, 31062 Toulouse Cedex 9, France

Abstract

Spinel oxide nanoparticles of $M_xCo_{2-x}MnO_4$ (M = Ni, Zn, Cu; 0 < x < 1) were prepared at 120°C by the inorganic polycondensation method. Phase composition and microstructure of each sample powder thus obtained were characterized by X-ray diffraction, X-ray fluorescence and scanning electron microscopy. Nanoparticles are well crystallized and uniformly distributed in both shape and size. Colloidal dispersions were stabilized in a low cost and environmentally friendly solvent solution. Spinel oxide thin films were then deposited on glass substrates by using the dip-coating technique. Their optical properties were measured in the 300–1100 nm wavelength range. Thin films show extremely good absorbance in the ultra-violet and blue regions. The highest absorbance observed in the red region was for x = 0.15 in zinc. A smaller direct band gap was determined when a low amount of doping M element was introduced in the cobalt and manganese spinel oxide material.

Keywords: Ceramics; Spinel oxide; Colloidal dispersion; Thin films; Optical properties.

*corresponding author: tenailleau@chimie.ups-tlse.fr

1. Introduction

Transition metal oxides (TMO) with the spinel structure (represented by the general formula unit AB_2O_4, with A^{2+} ions and B^{3+} ions) have always attracted intensive interests due to their rich and various physical phenomena such as metal-insulator transition, superconductivity, ferromagnetism [1-4]. Among all of the possible coatings, $(Mn,Co)_3O_4$ spinel is regarded as one of the most promising candidate for applications in integrated multifunctional systems used in electronic devices, catalysis, (photo-)electrochemistry, chemical sensors and fuel cells due, for instance, to its relatively high conductivity and compatible coefficient of temperature expansion with metallic interconnects [5,6]. Furthermore, spinel oxides are important TMO semiconductors that exhibit a rich variety of electrical, magnetic and optical properties and their performances can be further improved by doping with a wide range of transition metal cations [7-10]. Presently, many physical and chemical techniques such as screen printing [11], Radio-Frequency (RF) sputtering deposition [12], laser molecular beam epitaxy [13] and chemical solution deposition (CSD) methods [14,15], spin spray [16] and sol-gel technique [17,18] have been used to prepare spinel oxide thin films.

Recently, we synthesized a series of pure manganese and cobalt compounds by soft chemistry methods [17]. These p-type semiconducting materials also exhibit interesting optical properties with very high ultraviolet (UV) and early visible absorption, and almost transparency in the infrared (IR) region. We also showed that $MnCo_2O_4$ exhibits the highest conductivity from the Mn-Co-O spinel family [19]. $MnCo_2O_4$ is therefore of particular importance and its band gap (E_g = 2.1 eV) can be adjusted with doping.

A few works were devoted to the study of the optical properties of Mn-Co-Ni-O thin films. For instance, Dannenberg et al. (1999) studied the infrared optical properties of $Mn_{1.56}Co_{0.96}Ni_{0.48}O_4$ thin films deposited by RF sputtering method on silicon substrate. The films have an optically transparent window from 6 to 14 µm [20]. Zhou et al. (2014) investigated the UV-VIS-NIR and infrared optical constants by spectroscopic ellipsometry for the as-grown and post-annealed $Mn_{1.4}Co_{1.0}Ni_{0.6}O_4$ films. These can be used for the development of optoelectronic devices [12]. Gao et al. (2014) prepared $Mn_{1.56}Co_{0.96}Ni_{0.48}O_4$ thin films on Al_2O_3 substrate by the CSD method. The thin film band gap was calculated to be about 0.64 eV [14]. While Co_3O_4 doped with Ni or Zn can be a useful p-type photoelectrode for replacing NiO in dye sensitized solar cells [21], doping Mn-Co-O spinel oxides with Cu and Ni can also improve sintering characteristics and electrical conductivity [5].

In this study, we used the inorganic polycondensation method to synthesize pure crystalline nanoparticles at low temperature and then used the low cost effective dip-coating technique for preparing the corresponding compositional thin films [17]. Structural and microstructural characteristics of sample powders were studied and the optical properties of the spinel oxide thin films were investigated in detail.

2. Experimental details

2.1. Powder preparation

Samples of $Ni_xCo_{2-x}MnO_4$ (NCM), $Zn_xCo_{2-x}MnO_4$ (ZCM) and $Cu_xCo_{2-x}MnO_4$ (CCM) were prepared and their main features are listed in Table 1.

Spinel oxide nanoparticles of NCM, ZCM and CCM were prepared by a simple method based on the inorganic polycondensation of particles [17,22]. Metal (II) sulfates were dissolved in distilled water with a fixed concentration (C = 0.3 M) of solution. For a high

saturation of solution, the free enthalpy can be decreased by the formation of individual nuclei within a suspension of a homogenous phase which characterizes the germination process. The system will then change until reaching an equilibrium by a growing step that will generate primary particles. The final particle size strongly depends on the germination process. We thus performed a detailed study on the essential paramaters that control the formation of such particles during the first stages of precipitation. Particle growth can be limited by a strong dilution. Increasing the alkaline solution concentration can increase supersaturation, drive to nucleation and decrease the particle size. A low dielectric constant, by introducing ethanol in the solution for instance, can also have similar effects.

Therefore, solutions were voluntarily close to the saturation point in order to promote germination before the growth of nanoparticles. The metal salt solutions were quickly mixed in a larger volume of LiOH solution (V_{salt}/V_{buffer} = 0.7) with pH ~ 12 and left under stirring for 90 minutes at room temperature to form a precipitate. The solution was then filtered and washed several times with distilled water by centrifugation in order to remove any interfering ions. A following step of reflux with distilled water at 120°C for two hours was necessary to provide oxygen to the alkali hydroxide precursors and form metal oxide nanoparticles. Pure crystalline oxide powders were obtained after drying in air.

2.2. Thin film preparation

Thin films were prepared by the dip-coating technique, using an azeotrope solution (mixture of absolute ethanol and ultra-pure water) as the solvent. Powders were dispersed in a solution set at a pH = 6 by ultrasonication. After several washes in absolute ethanol, colloidal suspensions (sols) of pure spinel oxide nanoparticles were stabilized for a few months in the azeotrope solution which is also favorable for a homogeneous sample deposition on metal or glass substrate. Thin films were deposited by dip-coating into the sols and withdrawing the substrate at a constant rate of 200 mm per minute. The adhesion on glass is poor without annealing. But the substrate is fully covered by a homogenous layer of oxide nanoparticles. The film thickness (minimum of 300 nm) can be adjusted by repeating this sequence and after letting it dry in air for one minute at room temperature in between each dip-retrieval sequence.

2.3. Characterization

X-ray diffraction (XRD) data were recorded on a Bruker D4-ENDEAVOR diffractometer using CuKα (λ = 1.54060 Å) radiation (40 kV, 40 mA) and collected over the 10° < 2θ < 100° range at room temperature, with a 0.02° step scan and 3.6 s/step.

The atomic percentages for each powder sample were probed by X-ray fluorescence (XRF) using a Bruker S2 Ranger spectrometer.

Thin film surface morphologies were examined using a JEOL 6700F Scanning Electron Microscope (SEM) with a Field Emission Gun (FEG) operated from 0.5 to 30 kV, with a resolution of 1.0 nm at 15 kV and 2.2 nm at 1 kV.

Transmittance $T(\lambda)$ and reflectance $R(\lambda)$ measurements were carried out at room temperature by using a BENTHAM 605 UV-vis-NIR spectrophotometer in the 300-1100 nm wavelength region (step scan of 5 nm).

2.4. Light absorption determination

The spinel oxide thin films were deposited on transparent substrate such as glass in the studied 300-1100 nm wavelength region.

For a film thickness d, the absorption coefficient α was computed from the experimental measurements of the transmittance $T(\lambda)$ and reflectance $R(\lambda)$ by using the following formulae [23,24]:

$$T = \frac{(1-R)^2 e^{-\alpha d}}{1-R^2 e^{-2\alpha d}} \quad (1)$$

$$\alpha = -\frac{1}{d} ln\left[\frac{\sqrt{(1-R)^4 + 4T^2R^2} - (1-R)^2}{2TR^2}\right] \quad (2)$$

3. Results and discussion

3.1. XRD analysis

X-ray diffraction (XRD) patterns of all oxide powders are shown in Figure 1. Each pattern can be indexed with a single spinel oxide phase structure of cubic symmetry (*Fd-3m* space group). Wide peak shapes are characteristics of nanometer scale size crystallites. The overall background is quite high due to transition metal fluorescence with the Cu wavelength used for XRD. No significant change is observed in the peak intensities with metal substitution as can be seen for instance when comparing each (311) strongest line. For copper containing spinel oxides, of CCM general composition, while CCM15 powder is pure and crystallizes also with a cubic structure, the next compositions show extra peaks which were attributed to a Cu-Co-O structure phase for CCM30 and the addition of CuO for further doping, i.e. CCM60. These latter two materials (CCM30 and CCM60) were not further studied.

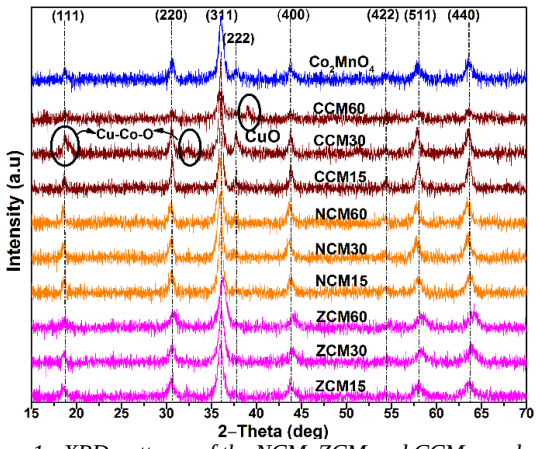

Figure 1 : XRD patterns of the NCM, ZCM and CCM powders, in comparison with Co_2MnO_4 (with Bragg peak indices written into brackets).

Table 1: $M_xCo_{2-x}MnO_4$ sample compositions and their main structural parameters. The last two samples contain also CuO.

M	x	Sample formula	Sample abbreviation	Calculated sample formula (from XRF data)	Lattice constant (nm)	Crystal size (nm)
---	0	Co_2MnO_4	---	$Co_{2.01}Mn_{0.99}O_4$	0.8268(1)	27(5)
Zn	0.15	$Zn_{0.15}Co_{1.85}Mn_{1.00}O_4$	ZCM15	$Zn_{0.16}Co_{1.84}Mn_{1.00}O_4$	0.8274(10)	14(3)
	0.30	$Zn_{0.30}Co_{1.70}Mn_{1.00}O_4$	ZCM30	$Zn_{0.32}Co_{1.68}Mn_{1.00}O_4$	0.8250(5)	12(2)
	0.60	$Zn_{0.60}Co_{1.40}Mn_{1.00}O_4$	ZCM60	$Zn_{0.63}Co_{1.37}Mn_{1.00}O_4$	0.8209(1)	11(4)
Ni	0.15	$Ni_{0.15}Co_{1.85}Mn_{1.00}O_4$	NCM15	$Ni_{0.16}Co_{1.85}Mn_{0.99}O_4$	0.8243(7)	15(1)
	0.30	$Ni_{0.30}Co_{1.70}Mn_{1.00}O_4$	NCM30	$Ni_{0.32}Co_{1.68}Mn_{1.00}O_4$	0.8271(3)	15(3)
	0.60	$Ni_{0.60}Co_{1.40}Mn_{1.00}O_4$	NCM60	$Ni_{0.62}Co_{1.39}Mn_{0.99}O_4$	0.8295(9)	14(4)
Cu	0.15	$Cu_{0.15}Co_{1.85}Mn_{1.00}O_4$	CCM15	$Cu_{0.15}Co_{1.84}Mn_{1.01}O_4$	0.8271(3)	25(2)
	0.30	$Cu_{0.30}Co_{1.70}Mn_{1.00}O_4$	CCM30	---	---	---
	0.60	$Cu_{0.60}Co_{1.40}Mn_{1.00}O_4$	CCM60	---	---	---

The lattice constants extracted from the XRD data and sample stoichiometries as determined by XRF analysis are reported in Table 1. The cell parameter increases with the addition of nickel, because the radius of the Ni^{2+} ion is larger than that of Mn^{2+} and Co^{2+} [25]. Besides, Ni^{2+} shows an octahedral site preference just like Mn^{3+}, Mn^{4+} and Co^{3+} while Mn^{2+} and Co^{2+} show a tetrahedral site preference. On the contrary, the lattice constant of ZCM compounds decrease with increasing Zn content due to the tetrahedral site preference for the larger Zn^{2+} ions [26]. Full width at half maximum (*FWHM*) of the (311) peak for each cubic phase is about 0.01 rad, corresponding to an averaged crystallite size of ~13 nm estimated by Scherrer's equation $D = \frac{K\lambda}{\beta cos\theta}$, where λ is the X-ray wavelength, K = 0.94 (a dimensionless shape factor), β the *FWHM* for the (311) diffraction peak and θ the Bragg diffraction angle, while making the assumption of perfectly spherical particles.

The average crystallite size for each composition was then calculated from the (311) XRD peak (see Table 1). For the NCM materials, crystallite sizes are very similar (~15 nm in diameter) but for the ZCM samples, the average crystallite size decreases with increasing the Zn concentration. This may arises from a larger number of Zn^{2+} ions, having a small ionic radius, replacing Mn^{2+} ions [27].

3.2. Morphological analysis

Particle morphology was examined by direct observation using Scanning Electron Microscope (SEM). As an example, the micrographs of NCM15, ZCM15 and CCM15 powders are given in Figure 2(a)-(c), respectively. An average nanoparticle diameter was determined by measuring, for each sample, the size of twenty particles observed on the SEM micrograph by using the ImageJ software. Diameters of 35 nm, 30 nm and 50 nm were determined for NCM15, ZCM15 and CCM15, respectively. These particles are made up of many smaller crystallites, corresponding to the crystallite size determined by X-ray diffraction. Salek et al. (2012) [17,22] and Park et al. (2013) [5] reported similar rose-like morphology for Co_2MnO_4 and $Ni_{0.2}Co_{1.4}Mn_{1.4}O_4$.

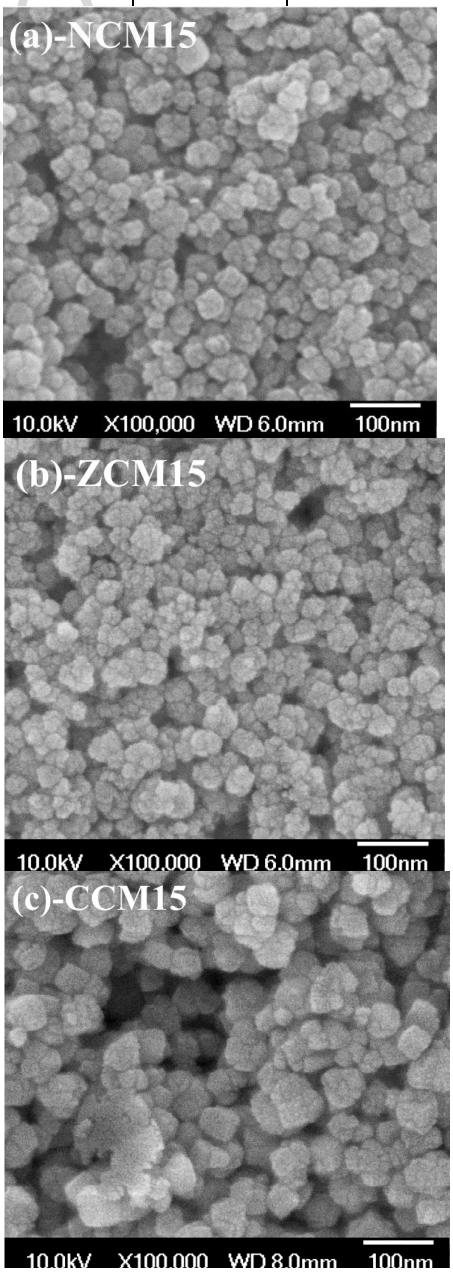

Figure 2: SEM micrographs of the (a)-NCM15, (b)-ZCM15 and (c)-CCM15 powders

The thinnest layer obtained after one dip-coating is close to 300 nm. Figure 3 shows the surface morphology

of a thin film obtained after three dip-coating sequences at room temperature and observed by SEM. The substrate is then well and homogenously covered by the oxide thin film over the entire surface area. A thickness of ~1 µm is measured after three dip-coating sequences, as can be seen on the cross section image in Figure 3.

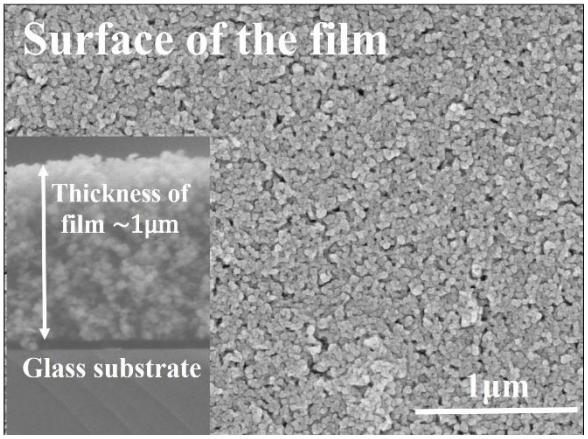

Figure 3: SEM of the surface and average thickness (cross section view) of the thin film obtained after three dip-coatings.

3.3. Optical properties

The spectral variations of transmittance $T(\lambda)$ and $R(\lambda)$ of thin films measured at room temperature in the 300 - 1100 nm wavelength range and for a film thickness of ~1µm are show in Figure 4. The reflectance is low ($R(\lambda) < 10\%$) over the whole spectral range. Thin films exhibit high transparencies in the infrared spectral region. The curves of absorbance, which were obtained following the simplified relation $A(\lambda) = 1 - T(\lambda) - R(\lambda)$, are also given in the inset of Figure 4. The overall variations are very similar for all compositions. The absorbance spectrum exhibits two strong absorption bands at around 450 nm and 750 nm in wavelengths for all the samples. The first front of absorbance in the UV region remains very high for all Ni, Cu or Zn contents. While the absorbance of metal doped-$MnCo_2O_4$ is increased in the visible region, a blueshift of the absorbance in this region is observed with the increase of Zn or Ni concentration. Also, the second front of absorbance at around 700 nm gradually decreases from Zn (ZCM15) to Cu (CCM15) and Ni (NCM15). Zn^{2+} (d^{10}) is concentrated on the tetrahedral sites while Cu^{2+} (d^9) and Ni^{2+} (d^8) are essentially situated on the octahedral sites. However, Ni^{2+}, Cu^{2+} and Cu^{+} were also reported on the tetrahedral sites [15,28].

The spinel oxides band gaps can be determined following Tauc's relation [29]:

$$\alpha = \frac{C}{h\nu}\left(h\nu - E_g\right)^m \qquad (3)$$

Where α is the absorption coefficient, $h\nu$ the photon energy, C an energy independent constant, E_g the optical band gap and m is a constant.

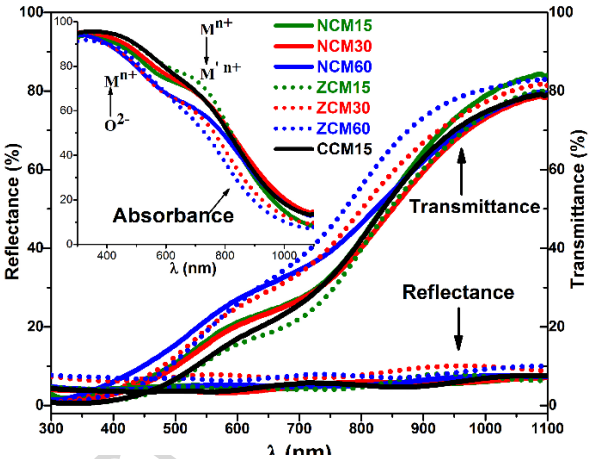

Figure 4: Spectral variations of the transmittance, reflectance and deduced absorbance for NCM, ZCM and CCM15 thin films.

3.4. Band gap determination

In solid state physics, the band gap is a major factor related to the electrical conductivity of a solid. The band gap is usually determined by studying its optical transmission and reflection spectra in the near ultraviolet to near infrared (UV-Vis-IR) spectral range or ellipsometric spectra as well as density functional theory (DFT) [30].

The m exponent, extracted from Tauc's power-law behavior (equation (3)) is a constant equal to 2 or 3 for indirect allowed or forbidden transitions, respectively while m is equal to 1/2 or 3/2 for direct allowed or forbidden transitions, respectively [31,32]. The absorption coefficient α spectra of the NCM, ZCM and CCM15 thin films are shown in Figure 6. The two strong absorption bands are evidenced for each film in the region between 300 and 800 nm. Those absorption bands arise from a linear combination of these one-electron transitions. The two peaks observed for each spectrum of the absorption coefficient α (Figure 5) corresponds to the two peaks in the spectrum of the absorbance (inset of Figure 4).

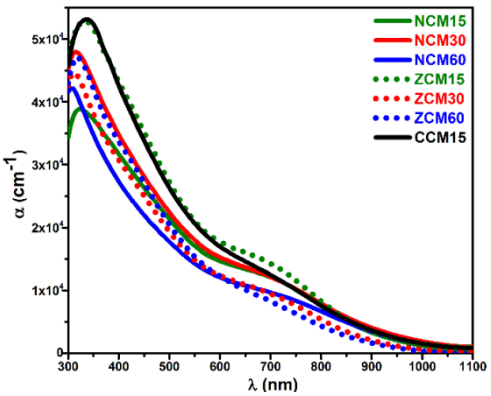

Figure 5: The spectral distribution of the absorption coefficient of NCM, ZCM and CCM15 thin films.

Equation (3) can be rewritten as:

$$\ln\left(\alpha h\nu\right) = m \ln\left(h\nu - E_g\right) \qquad (4)$$

$$\frac{d[\ln(\alpha h\nu)]}{d(h\nu)} = \frac{m}{h\nu - E_g} \qquad (5)$$

The type of transition can be obtained from the m value in the equation (4). Here, m is as the slope of the ln ($\alpha h\nu$) vs ln ($h\nu$ - E_g) curve (Figure 7). The value of E_g is determined by plotting $\frac{d[ln(\alpha h\nu)]}{d(h\nu)}$ as a function of $h\nu$ (see Figure 6). The strongest peaks there observed at the particular energy values give a good approximation of the optical band gap E_g. Two values of E_g are evidenced for each composition.

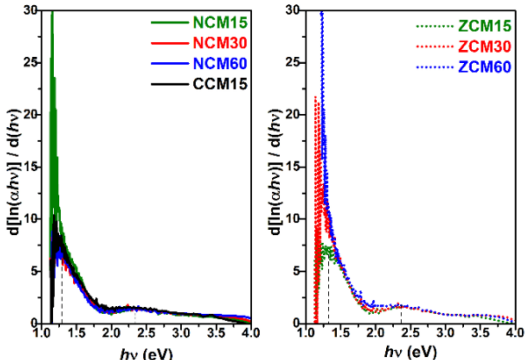

Figure 6: Plot of d [ln(αhν)] / d(hν) as a function of photon energy hυ for the NCM, ZCM and CCM15 thin films.

These E_g values were used to plot ln ($\alpha h\nu$) as a function of ln ($h\nu - E_g$) in order to determine the m value (Figure 7). Each sample shows two values of optical band gap and the linear fit always gives the same slope value of 1/2, which indicates that direct transitions occur in the films of NCM, ZCM and CCM15.

In order to determine precisely the optical band gap E_g value, we plotted $(\alpha h\nu)^2$ as a function of photon energy $h\nu$ in Figure 8. The optical band gaps were determined by extrapolation of the linear portion of the peaks for each plot to $(\alpha h\nu)^2 = 0$.

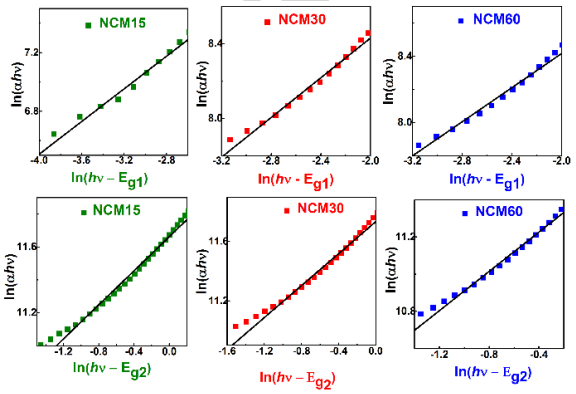

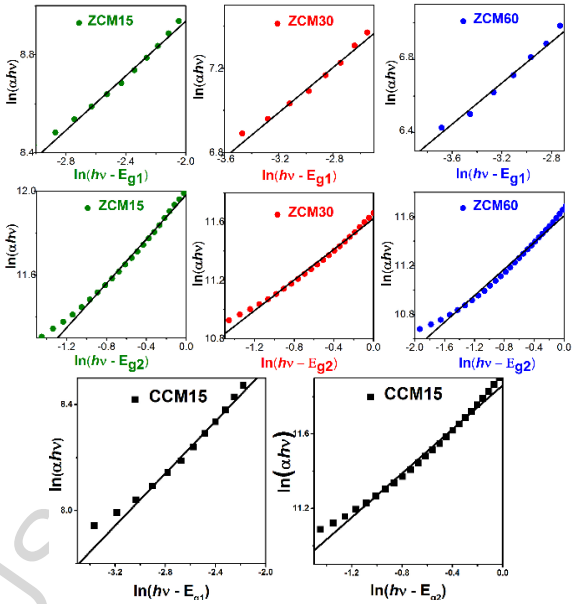

Figure 7: Plots of ln (αhυ) as a function of ln (hυ - E_g) for NCM, ZCM and CCM15 thin films.

Again, there are two energy gaps for each composition as seen in Figure 8. The values of E_{g1}, corresponding to the smallest gap value and the largest absorption band at about 750 nm, can be related to an energy transition between two metal cations. The values of E_{g2}, corresponding to the largest gap value and the first absorption band in the measured area (at about 450 nm), can be related to an energy transition from the oxygen anion to the metal cation [17,33,34].

Table 2 lists the values of the band gaps obtained from the present study, which are in good agreement with those reported in the literature for similar compositions [17,35-39]. The substitution of 15 at.% Co by a higher atomic number transition metal M of the same period in $M_xCo_{2-x}MnO_4$ decreases the first band gap E_{g1} while E_{g2} remains similar (E_{g1} = 1.37/1.39 eV for NCM15, ZCM15 and CCM15 in comparison with E_{g1} = 1.48 eV for $MnCo_2O_4$). Doping by a metal element M with a higher atomic number than for Co (and Mn) contributes to more localized orbitals and less overlapping. The interaction with the oxygen anion is also lowered with doping, which can explain the E_{g2} gap increase due to charge transfer from the oxygen 2p orbitals to the metal d orbitals. The presence of M^{2+} cations on the octahedral sites (with Ni^{2+} and Cu^{2+}) induces the manganese oxidation on this site and contributes to the material conductivity increase. The valence band, which is essentially composed of metal orbitals defining the highest occupied level for the first E_{g1} band gap, is filled in with more electrons as the doping element atomic number is increased and this band gap decreases. In the case of Zn^{2+}, which is substituted to Co^{2+} on the tetrahedral site of the spinel oxide, there is no impact on the overall charge neutrality, and in particular on the octahedral site cation distribution, but E_{g1} tends to increase with the amount of Zn^{2+}, as the tetrahedral orbital are more localized. Both band gaps (E_{g1} and E_{g2}) generally increase with a larger amount of doping element. Finally, our pure materials synthesized and deposited as thin and homogenous layers on a substrate by an easy processing technique

show two direct band gaps that can be adjusted through simple doping.

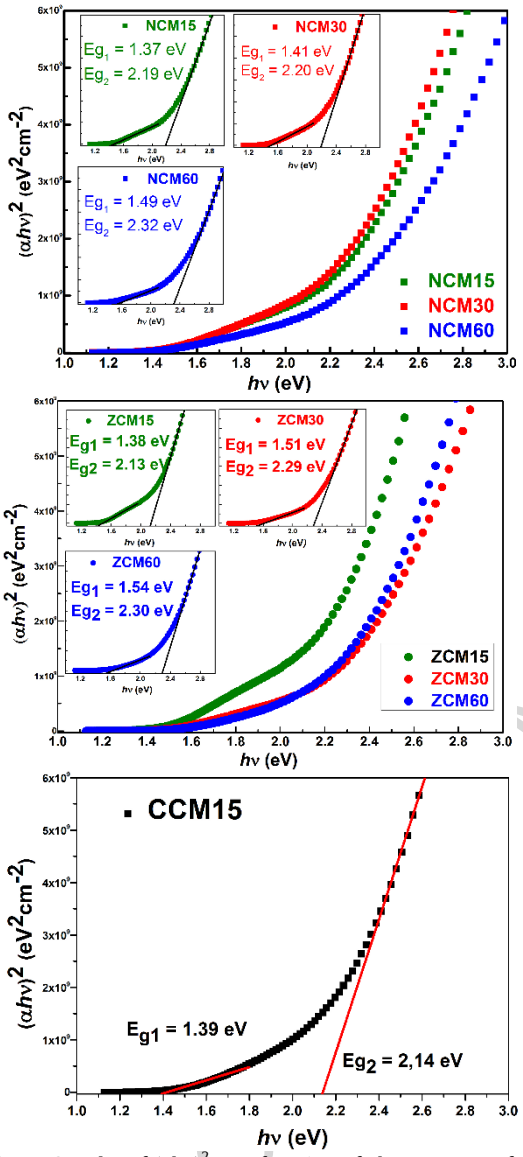

Figure 8 : Plot of $(\alpha h\nu)^2$ as a function of photon energy for NCM, ZCM and CCM15 thin films.

Table 2: The optical band gaps of the NCM, ZCM and CCM15 thin films determined in this work and compared with values reported in the literature.

Compound	E_{g1} (eV)	E_{g2} (eV)	Ref
NCM15-$Ni_{0.16}Co_{1.85}Mn_{0.99}O_4$	1.37	2.19	present work
NCM30-$Ni_{0.32}Co_{1.68}Mn_{1.00}O_4$	1.41	2.20	
NCM60-$Ni_{0.62}Co_{1.39}Mn_{0.99}O_4$	1.49	2.32	
ZCM15-$Zn_{0.16}Co_{1.84}Mn_{1.00}O_4$	1.38	2.13	
ZCM30-$Zn_{0.32}Co_{1.68}Mn_{1.00}O_4$	1.51	2.29	
ZCM60-$Zn_{0.63}Co_{1.37}Mn_{1.00}O_4$	1.54	2.30	
CCM15-$Cu_{0.15}Co_{1.84}Mn_{1.01}O_4$	1.39	2.14	
Co_2MnO_4	1.48	2.13	[17,36,37]
Zn-Co-O	-	2.30	[35,36]
$Ni_{0.6}Co_{1.0}Mn_{1.4}O_4$	0.51	-	[38]
$Ni_{0.48}Co_{0.96}Mn_{1.56}O_4$	0.64	-	[39]

4. Conclusions

Spherical nanoparticles (30 nm < diameter < 50 nm) of single cubic spinel oxide phases $M_xCo_{2-x}MnO_4$ (M = Ni, Zn, Cu; 0 < x < 1) were synthesized by a simple method based on inorganic polycondensation. Homogenous thin films were prepared at room temperature by the stabilization of colloidal suspensions using only water and ethanol as solvents. The optical properties of spinel oxide thin films show two strong absorption bands for each composition at the UV front and close to 700 nm in wavelength. Direct bands gaps were determined. The lowest band gap was obtained for $Ni_{0.15}Co_{1,85}MnO_4$ (close to the one determined for the same concentration of copper and zinc). Both band gaps increase with further doping. These optical properties of stable and environmentally friendly p-type semiconducting compounds could be useful for various applications including (photo-)catalysis, (photo-)electrochemistry and solar cells…

Acknowledgments

The Vietnamese government and University of Sciences and Technology in Hanoi (USTH) program are thanked for financial contribution to the PhD student salary (3811/QD-BGDDT grant number delivered on the September 12th 2013).

References

[1] C.L. Lu, X. Chen, S. Dong, K.F. Wang, H.L. Cai, J.M. Liu, D. Li, Z.D. Zhang, Ru-doping-induced ferromagnetism in charge-ordered La0.4Ca0.6MnO3, Phys. Rev. B 79 (2009) 2451051-2451056.

[2] K. Jin, N.P. Butch, K. Kirshenbaum, J. Paglione, R.L. Greene, Link between spin fluctuations and electron pairing in copper oxide superconductors, Nature 476 (2011) 73-75.

[3] C.J. Zhang, H. Oyanagi, Local lattice instability and superconductivity in La1.85Sr0.15Cu1-xMxO4 (M = Mn, Ni and Co), Phys. Rev. B 79 (2009) 0645211-0645218.

[4] A. Zimmers, L. Aigouy, M. Mortier, A. Sharoni, S. Wang, K.G. West, J.G. Ramirez, I.K. Schuller, Role of Thermal Heating on the Voltage Induced Insulator-Metal Transition in VO2, Phys. Rev. Lett. 110 (2013) 0566011-0566015.

[5] B.-K. Park, J.-W. Lee, S.-B. Lee, T.-H. Lim, S.-J. Park, C.-O. Park, R.-H. Song, Cu-and Ni-doped Mn1.5Co1.5O4 spinel coatings on metallic interconnects for solid oxide fuel cells, Int. J. Hydrogen Energy 38 (2013) 12043-12050.

[6] Y. Xu, Z. Wen, S. Wang, T. Wen, Cu doped Mn–Co spinel protective coating on ferritic stainless steels for SOFC interconnect applications, Solid State Ionics 192 (2011) 561-564.

[7] L. He, Z. Ling, Studies of temperature dependent ac impedance of a negative temperature coefficient Mn-Co-Ni-O thin film thermistor, Appl. Phys. Lett. 98 (2011) 2421121-2421123.

[8] L. He, Z.Y. Ling, Electrical conduction of intrinsic grain and grain boundary in Mn-Co-Ni-O thin film thermistors: Grain size influence, J. Appl. Phys. 110 (2011) 0937081-0937086.

[9] J. Wu, Z. Huang, Y. Hou, Y. Gao, J. Chu, Variation in hopping conduction across the magnetic transition in spinel Mn1.56Co0.96Ni0.48O4 films, Appl. Phys. Lett. 96 (2010) 0821031-0821034.

[10] Y.Q. Gao, Z.M. Huang, Y. Hou, J. Wu, Y.J. Ge, J.H. Chu, Optical properties of Mn1.56Co0.96Ni0.48O4 films studied by spectroscopic ellipsometry, Appl. Phys. Lett. 94 (2009) 0111061-0111063.

[11] S.A. Kanade, V. Puri, Composition dependent resistivity of thick film Ni(1−x)CoxMn2O4 ($0 \leq x \leq 1$) NTC thermistors, Mater. Lett. 60 (2006) 1428-1431.

[12] W. Zhou, J. Wu, C. Ouyang, Y.Q. Gao, X.F. Xu, Z.M. Huang, Optical properties of Mn-Co-Ni-O thin films prepared by radio frequency sputtering deposition, J. Appl. Phys. 115 (2014) 0935121-0935127.

[13] G. Ji, A. Chang, J. Xu, H. Zhang, J. Hou, B. Zhang, P. Zhao, Low-temperature (<300°C) growth and characterization of single-[100]-oriented Mn–Co–Ni–O thin films, Mater. Lett. 107 (2013) 103-106.

[14] Y.Q. Gao, Z.M. Huang, Y. Hou, J. Wu, W. Zhou, L.B. Zhang, J.H. Chu, Infrared optical properties of Mn1.56Co0.96Ni0.48O4 thin films prepared by chemical solution deposition, Appl. Phys. A 114 (2014) 829-832.

[15] J. Wu, Z. Huang, W. Zhou, C. Ouyang, Y. Hou, Y. Gao, R. Chen, J. Chu, Investigation of cation distribution, electrical, magnetic properties and their correlation in Mn2-xCo2xNi1-xO4 films, J. Appl. Phys. 115 (2014) 1137031-1137038.

[16] S.W. Ko, J. Li, N.J. Podraza, E.C. Dickey, S. Trolier-McKinstry, Spin Spray-Deposited Nickel Manganite Thermistor Films For Microbolometer Applications, J. Am. Ceram. Soc. 94 (2011) 516-523.

[17] G. Salek, P. Dufour, S. Guillemet-Fritsch, C. Tenailleau, Sustainable low temperature preparation of Mn3−xCoxO4 ($0 \leq x \leq 3$) spinel oxide colloidal dispersions used for solar absorber thin films, Mater. Chem. Phys. 162 (2015) 252-262.

[18] J. Vince, A. Šurca Vuk, U.O. Krašovec, B. Orel, M. Köhl, M. Heck, Solar absorber coatings based on CoCuMnOx spinels prepared via the sol–gel process: structural and optical properties, Sol. Energy Mater. Sol. Cells 79 (2003) 313-330.

[19] H. Bordeneuve, C. Tenailleau, S. Guillemet-Fritsch, R. Smith, E. Suard, A. Rousset, Structural variations and cation distributions in Mn3−xCoxO4 ($0 \leq x \leq 3$) dense ceramics using neutron diffraction data, Solid State Sci. 12 (2010) 379-386.

[20] R. Dannenberg, S. Baliga, R.J. Gambino, A.H. King, A.P. Doctor, Infrared optical properties of Mn1.56Co0.96Ni0.48O4 spinel films sputter deposited in an oxygen partial pressure series, J. Appl. Phys. 86 (1999) 2590-2601.

[21] C.C. Mercado, A. Zakutayev, K. Zhu, C.J. Flynn, J.F. Cahoon, A.J. Nozik, Sensitized Zinc–Cobalt–Oxide Spinel p-Type Photoelectrode, J. Phys. Chem. C 118 (2014) 25340-25349.

[22] G. Salek, S. Guillemet-Fritsch, P. Dufour, C. Tenailleau, A Simple Preparation Process of Pure Mn3-xCoxO4 (x = 1, 1.5 and 2) Desert Rose-Like Nanoparticles and Their Optical Properties, Int. J. Chem. 4 (2012) 44-53.

[23] P.J. Dean, D.G. Thomas, Intrinsic Absorption-Edge Spectrum of Gallium Phosphide, Phys. Rev. 150 (1966) 690-703.

[24] D.K. Schroder, Semiconductor Material and Device Characterization, Wiley-Interscience, 2006.

[25] R.D. Shannon, Revised effective ionic radii and systematic studies of interatomic distances in halides and chalcogenides, Acta Crystallogr. Sect. A 32 (1976) 751-767.

[26] A. Navrotsky, O.J. Kleppa, The thermodynamics of cation distributions in simple spinels, J. Inorg. Nucl. Chem. 29 (1967) 2701-2714.

[27] R. Arulmurugan, B. Jeyadevan, G. Vaidyanathan, S. Sendhilnathan, Effect of zinc substitution on Co–Zn and Mn–Zn ferrite nanoparticles prepared by co-precipitation, J. Magn. Magn. Mater. 288 (2005) 470-477.

[28] A.V. Salker, S.M. Gurav, Electronic and catalytic studies on Co1−xCuxMn2O4 for CO oxidation, J. Mater. Sci. 35 (2000) 4713-4719.

[29] J. Tauc, Amorphous and liquid semiconductors, in: J. Tauc (Ed.), Amorphous and liquid semiconductors, London and New York, 1974, pp. 175.

[30] N.J. Podraza, W. Qiu, B.B. Hinojosa, H. Xu, M.A. Motyka, S.R. Phillpot, J.E. Baciak, S. Trolier-McKinstry, J.C. Nino, Band gap and structure of single crystal BiI3: Resolving discrepancies in literature, J. Appl. Phys. 114 (2013) 0331101-0331109.

[31] A.A.M. Farag, I.S. Yahia, Structural, absorption and optical dispersion characteristics of rhodamine B thin films prepared by drop casting technique, Opt. Commun. 283 (2010) 4310-4317.

[32] A.A.M. Farag, M. Fadel, Optical absorption and dispersion analysis of nanocrystalline perylene-3,4,9,10-tetracarboxylic-3,4,9,10-

dianhydride film prepared by dip coating and its optoelectronic application, Opt. Laser Technol. 45 (2013) 356-363.

[33] S. Thota, A. Kumar, J. Kumar, Optical, electrical and magnetic properties of Co3O4 nanocrystallites obtained by thermal decomposition of sol–gel derived oxalates, Mater. Sci. Eng., B 164 (2009) 30-37.

[34] P.Y. Keng, B.Y. Kim, I.-B. Shim, R. Sahoo, P.E. Veneman, N.R. Armstrong, H. Yoo, J.E. Pemberton, M.M. Bull, J.J. Griebel, E.L. Ratcliff, K.G. Nebesny, J. Pyun, Colloidal Polymerization of Polymer-Coated Ferromagnetic Nanoparticles into Cobalt Oxide Nanowires, ACS Nano 3 (2009) 3143-3157.

[35] S. Kim, J.A. Cianfrone, P. Sadik, K.-W. Kim, M. Ivill, D.P. Norton, Room temperature deposited oxide p-n junction using p-type zinc-cobalt-oxide, J. Appl. Phys. 107 (2010) 1035381-1035385.

[36] F. Zasada, J. Gryboś, P. Indyka, W. Piskorz, J. Kaczmarczyk, Z. Sojka, Surface Structure and Morphology of M[CoM′]O4 (M = Mg, Zn, Fe, Co and M′ = Ni, Al, Mn, Co) Spinel Nanocrystals—DFT+U and TEM Screening Investigations, J. Phys. Chem. C 118 (2014) 19085-19097.

[37] S.M.A. Shibli, P.S. Arun, A.V. Raj, Exploration of octahedrally shaped MnCo2O4 catalyst particles for visible light driven photocatalytic water splitting reaction, RSC Advances 5 (2015) 19393-19399.

[38] W. Zhou, L. Zhang, C. Ouyang, J. Wu, Z. Huang, X.-f. Xu, Micro structural, electrical and optical properties of highly (220) oriented spinel Mn–Co–Ni–O film grown by radio frequency magnetron sputtering, Appl. Surf. Sci. 311 (2014) 443-447.

[39] Y.Q. Gao, Z.M. Huang, Y. Hou, J. Wu, J.H. Chu, Optical and electrical properties of Mn1.56Co0.96Ni0.48O4 thin films, in: C.W. Junhao Chu (Ed.), Eighth International Conference on Thin Film Physics and Applications, 2013, pp. 90680J90681-90680J90685.

Highlights

- Pure complex spinel oxide nanoparticles synthesis at low T
- Low cost method used to stabilize colloidal dispersions
- Preparation of homogenous light absorber thin films by dip-coating
- Adjustable optical properties and band gaps with the dopants